16th World Conference on Earthquake, 16WCEE 2017
Santiago Chile, January 9th to 13th 2017
Paper N° 4340 (Abstract ID)
Registration Code: S-K1464748820

Seismic Response of a Historical Unreinforced Masonry Building Damaged in the 2014 South Napa Earthquake

S. Günay[(1)], N. Giordano[(2)], S. Takhirov[(3)], K. M. Mosalam[(4)]

[(1)] *Project Scientist, University of California, Berkeley, USA, selimgunay@berkeley.edu*
[(2)] *PhD Candidate, Politecnico di Milano, Italy, nicola.giordano@polimi.it*
[(3)] *Structures Laboratory Manager, University of California, Berkeley, USA, takhirov@berkeley.edu*
[(4)] *Taisei Professor of Civil Engineering and PEER Director, University of California, Berkeley, USA, mosalam@berkeley.edu*

Abstract

Several unreinforced masonry buildings damaged during the 2014 South Napa earthquake, California, USA, were investigated after the earthquake. The numerical analyses conducted on a representative example are presented in this paper. The building is the Sam Kee laundry building, the oldest stone commercial building in Napa, built in 1875. The geometry of the building was accurately captured by a laser scanner. Using this geometry information and material data available in literature for similar buildings, a finite element model of the building was developed according to the equivalent frame approach and was subjected to nonlinear time history analyses. The investigated building was closely located to a strong motion station on Main Street, Napa, California. This record was used as seismic excitation input to the numerical model. Results of the conducted analyses accurately predicted the observed damage in the building which consisted of shear cracks and shear damage in the south and north walls and failure of piers from the east wall. Analysis results are used to describe the reasons of the observed damage.

Keywords: heritage building; laser scanning; nonlinear time history analysis, numerical modeling; unreinforced masonry;

1. Introduction

The Sam Kee laundry building, also known as the Pfeiffer building, is a historical building located at 1245 Main Street in Napa, California. It was built in 1875, and is considered as the oldest stone commercial building in Napa. As of 1880, the building was part of a brewery, which may have been the first brewery in Napa. It also contained a boarding house, a saloon, and a laundry. The building currently houses the Vintner's Collective, a wine tasting bar. It was added to the National Register of Historic Places Collection on October 1, 1974 [1] and was damaged in the 2014 South Napa earthquake. The building has a simple design topped by a decorative Italianate cornice. In the past years, the building underwent several restorations that resulted in different stone and grout materials in the masonry walls and in a variety of structural reinforcements.

2. Laser scan data

The conditions of the building in 1972 and right before the 2014 South Napa earthquake are presented in Fig. 1. The building was restored in the past and the masonry and grout materials used in these restorations differed from the original ones. The difference in the material used for the restorations is easily noticeable from the difference of colors in the photographs of Figs. 1a and b. To reinforce the building, the following measures were introduced in the past restorations: 1) two tie rods in the east-west direction with anchor plates right below the roof level and 2) four tie rods in the north-south direction at the first floor ceiling level as marked in Fig. 2a and as identified in the point cloud in Fig. 2b.

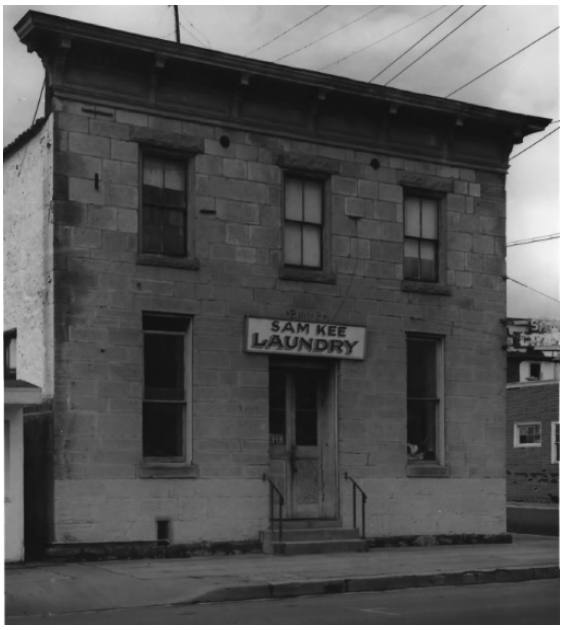

a) In 1972 (courtesy of National Register of Historic Places)

b) In 2014 (courtesy of Google Street View)

Fig. 1 – Front (east wall) view of the building before the earthquake

As mentioned above, the building was damaged during the 2014 South Napa earthquake. The south and north walls cracked right next to the east wall and several failure surfaces appeared in the east wall. As a result, a significant number of bricks from the façade fell down on the walkway right next to the building. Since the earthquake occurred at night time without any pedestrians on the streets, nobody was hurt. Photographs of the observed damage are presented in Figs. 3a to d.

a) Reinforcement measures

b) Anchorages of tie rods detected from laser scanning point cloud

Fig. 2 – Observations of the reinforcement measures and geometry estimates by the laser scanner

a) South wall

b) East and south walls

c) East and north walls

d) North wall

Fig. 3 – Damage observed in the building after the 2014 South Napa earthquake

The damaged condition of the building was scanned from three stations. A terrestrial laser scanner, namely Scan Station C10 from Leica Geosystems, was utilized in this study. The point clouds were stitched in the Cyclone

application [2] and the final point cloud is presented in Fig. 4a. The failure surfaces of the masonry walls are shown in Fig. 4b and the corresponding dislocations of the bricks are presented in Figs. 4c and d. The plots were generated in Matlab [3] and they present color contour maps of distances from a vertical plane (Deviations in North and East are positive).

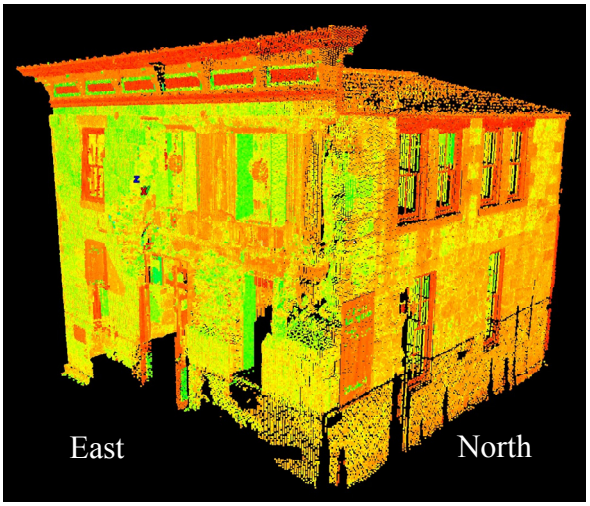

a) Point cloud

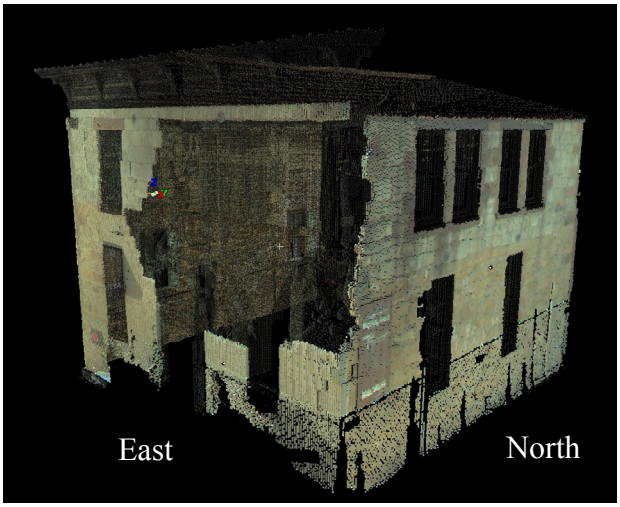

b) Outer skin showing failure surfaces of masonry walls

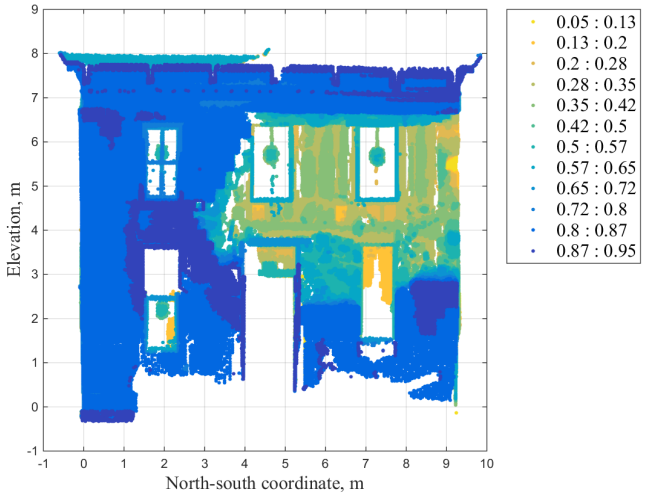

c) Contours of east-west deviations [m]: east wall

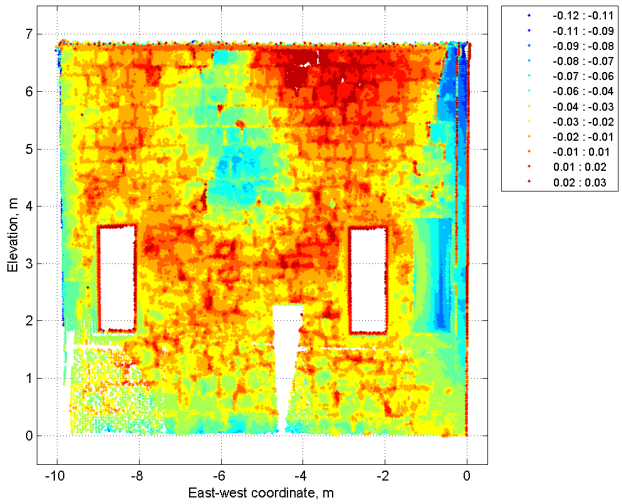

d) Contours of north-south deviations [m]: south wall

Fig. 4 – Data obtained from point clouds of the damaged building

3. Numerical model

In order to assess the structural performance of the building during the 2014 South Napa earthquake, a finite element model was developed according to the equivalent frame approach [4]. This method, inspired by the work of Tomazevic [5], consists of subdividing the masonry continuum into nonlinear deformable portions (piers and spandrels) connected at the intersections by rigid nodes [6]. Different formulations are available in the literature for the definition of the post-elastic behavior of these piers and spandrels [e.g. 7, 8]. In general, only the in-plane response is considered through uncoupled moment and shear plastic hinges, which take into account the geometry of the panel and the mechanical properties of the masonry in shear and compression. Some of the advantages of this method are: i) fast application for masonry buildings with regular openings, ii) reasonable computational cost due to the small number of elements, and iii) less problems related to convergence and stability of the solution compared to 2D or 3D continuum approaches [9]. The common usage of the equivalent

frame models is usually the nonlinear static pushover analysis as suggested by national and international guidelines, e.g. FEMA 306 [10] and CNR-DT 212/2013 [11].

With the objective of performing a nonlinear time history analyses (NLTHA) of the Laundry Building using the ground motion recorded in the vicinity of the building, the standard equivalent frame method was utilized in an enhanced manner using the OpenSees [12] framework. Particularly, the axial and biaxial-flexural responses were taken into account by the use of nonlinear displacement-based beam-column elements with fiber sections. On the other hand, shear damage potential has been included through concentrated shear springs with nonlinear force displacement relationships. P-Delta effects were also included in the analyses.

3.1 Geometry and mass distribution

The geometrical representation of the equivalent frame is shown in Fig. 4. In absence of project drawings, the dimensions of piers and spandrels have been extracted from the point cloud developed as a result of the laser scanning described in the previous section. The thickness of the walls, deduced from the collapsed parts of the façade, is assumed to be equal to 0.4 m. The cross-section length of the piers varies between 0.76 m (SP1) and 5.13 m (SP2). The cross-sectional depth values of the spandrels are between 0.46 m (ES4, ES5, andES6) and 3.12 m (SS1 andSS2).

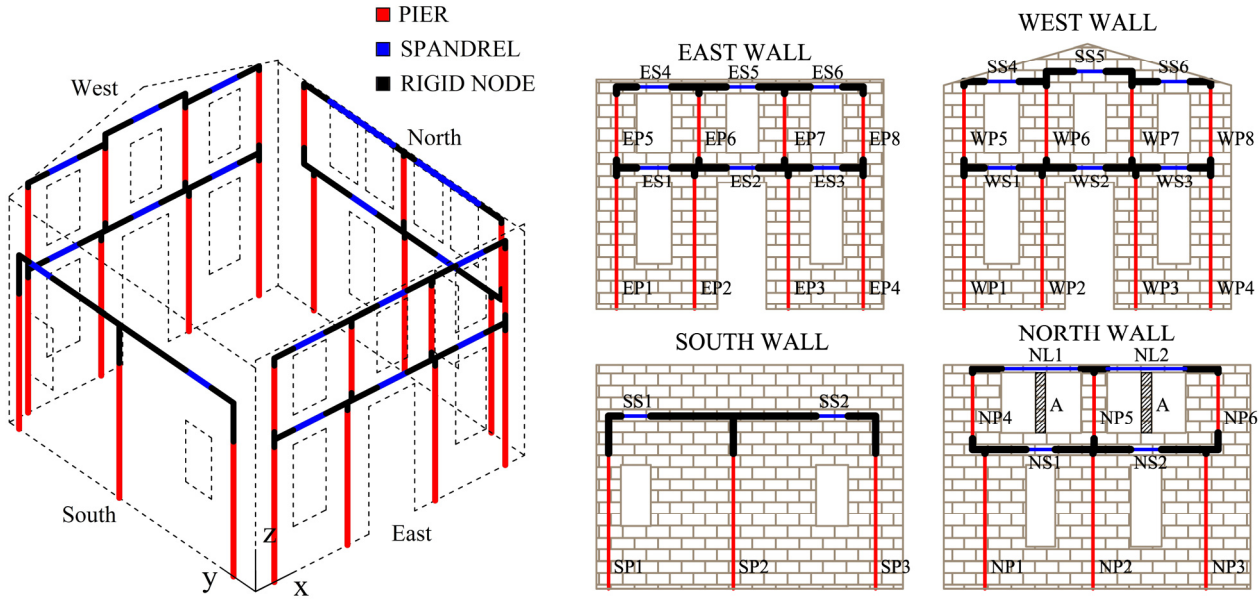

Fig. 4 – Equivalent frame model

Due to the small dimensions of the cross sections of piers A in Fig. 4, their contribution was neglected in the model. For the same reason, lintels NL1 and NL2 were modeled as truss elements. The connection between the four walls is ensured by imposing a rigid diaphragm constraint at the 1st floor and roof levels. In order to represent the mass distribution of the floor and the roof, two translational masses (directions x and y) and one rotational mass (about z) have been assigned to the central node of each diaphragm. The corresponding values are reported in Table 1 considering full slab-weight, superimposed dead load and 20% of the code specified live load. The masses of the walls have been directly assigned to the beam-column elements considering a masonry density equal to 1.8 t/m^3.

Table 1 – Coordinates of the rigid diaphragm center of mass and assigned masses

Level	x [m]	y [m]	z [m]	M_{dx} [t]	M_{dy} [t]	M_{rz} [t.m]
1st Floor	4.66	4.96	4.20	64.05	64.05	978.57
Roof	4.66	4.96	6.73	18.30	18.30	279.59

3.2 Nonlinear properties

As mentioned previously, piers and spandrels were modeled using nonlinear displacement-based beam-column elements in OpenSees (*dispBeamColumn*), [12] where the curvature distribution along its length is constant. Therefore, each pier and spandrel was subdivided into 6 elements to consider the variation of the curvature along the length of the pier or spandrel. P-Delta effects on the piers are considered using the geometric stiffness matrices. The nonlinear stress-strain relationship of the masonry is modeled with the *Concrete04* material in OpenSees [12]. This material model is based on the concrete model originally developed by Mander et al. [13], and is characterized by: i) parabolic branch in compression followed by a linear tension softening, ii) elastic-brittle behavior in tension, and iii) cyclic stiffness degradation. In absence of in-situ experimental tests, the mechanical parameters of the masonry have been taken from available data in the literature by Augenti et al. [14] resulting in a compressive strength f_m = 4 MPa and a Young's modulus E_m = 2222 MPa. The uniaxial stress-strain constitutive law adopted for the spandrels accounts for the horizontal bed joint sliding assuming an elastic-perfectly-plastic response, as suggested by FEMA 306 [10]. The utilized material model is assigned to each of each fiber, with 0.04m × 0.04m size, that define the sections of the nonlinear displacement-based beam-column elements.

Shear damage potential of masonry piers is considered using concentrated shear springs at the base of the elements, which are modeled using the so-called *zeroLength* elements of OpenSees [12]. The skeleton curve of these elements is defined according to [11] where the shear strength of the pier is defined as the minimum of $V_{u,dc}$ (failure by diagonal cracking) and $V_{u,bjs}$ (failure by bed joint sliding), defined according to [7] as follows:

$$V_{u,dc} = l \times t \times 1.5\tau_0 \left[1 + N / (l \times t \times 1.5\tau_0)\right]^{1/2} / b \quad (1)$$

$$V_{u,dc} = \mu N \quad (2)$$

where l is the length of the pier, t is the thickness, τ_0 = 0.1 MPa is the masonry shear strength, N is the axial load, b = l/h < 1.5 is the slenderness of the panel, and μ = 0.4 is the friction coefficient of the masonry. The maximum in-plane shear displacement is expressed in terms of percentage drift and is taken as 0.4% based on [11].

4. Seismic excitation recorded in vicinity of building

Station N016 from the USGS-NCSN strong motion network is within 350 meters from the analyzed building as presented in Fig. 5a. Because the accelerations recorded in this station are along the North-South and East-West directions, they were transformed to the accelerations along the two orthogonal directions of the building as shown in Fig. 5b. It is noted that the x and y directions in Fig. 5b are consistent with the x and y directions indicated in Fig. 4. The transformed accelerations are plotted in Fig. 6, while the response spectra of these accelerations are plotted in Fig. 7. The fundamental periods of vibration of the building are also marked on Fig. 7, where the corresponding spectral accelerations are 0.59g and 1.15g corresponding to the periods of 0.12 sec and 0.20 sec in the y and x directions, respectively.

5. Comparison of the analysis results with observed damage

NTHA of the developed model was conducted using Implicit Newmark integration with average acceleration (γ = 0.5, β = 0.25) and a time step Δt = 0.005 sec. Rayleigh damping was used to model viscous damping with the damping coefficients computed for 5% damping ratio in the fundamental periods of the building in both orthogonal directions. To overcome the convergence problems, adaptive switching of nonlinear solution algorithms and integration methods was utilized as described in [15, 16].

Time histories of base shear forces in the x and y directions of the building normalized by the weight are plotted in Fig. 8. It is observed that the spectral accelerations corresponding to the natural periods of the building in Fig. 7 are larger than the peak normalized base shears in Fig. 8, indicating that the base shear capacity of the building is reached in both directions. As expected, the base shear capacity in the y direction is higher than that in the x

direction (about 0.31/0.23 ≈ 1.35 times higher, refer to Fig. 8), mainly due to the large number of openings including doors in the x direction and the existence of mostly solid walls in the y direction. Global force-displacement relationships of the four walls, (north and south) in the y direction and (east and west) in the x direction, are plotted in Fig. 9. Differences in the response between south and north walls indicate the existence of torsion which is mainly caused by the stiffness differences of these two walls having different number of openings (6 windows in the north wall compared to only 2 windows in the south wall). It is observed that the stiffer south wall is subjected to larger forces in the elastic range of response, but is subjected to smaller drifts because of its higher strength. Both the east and west walls show degraded response consistent with the observed damage after the 2014 South Napa earthquake. The reason of having degraded response in the east and west walls along the x direction, while having more stable response in the north and south walls along the y direction, can be briefly explained by the demand to capacity ratios (1.15/0.23 = 5 in the x direction, which is much higher than that in the y direction, namely 0.59/0.31 = 1.9).

One observation that can be made from Fig. 9 is that the ratio of the sum of the capacities from the north and south walls to that from the east and west walls is around (2×300)/(2×150) = 2. This ratio differs from the 1.35 base shear capacity ratio observed from Fig. 8. There are two possible reasons for this difference: (1) due to torsion, the capacities are not reached simultaneously in the north and south walls (nor in the east and west walls) at any instant during the time history, (2) orthogonal walls contribute slightly to the base shear capacity.

As observed in Figs. 2 and 4, the piers EP7 and EP8 failed during the 2014 South Napa earthquake. The in-plane force-displacement relationships shown in Fig. 10 indicate that the strength of these piers has been reduced considerably and the response is significantly degraded, which explain the reason of these collapses. To investigate the reason of having EP8 collapsed, while EP5 on the other corner remaining intact, the out-of-plane accelerations that these two piers experienced are compared in Fig. 11, from which it is observed that these accelerations have similar amplitudes. Not plotted here, the interstory drifts in the out-of-plane direction (i.e. along y direction) are also similar. On the other hand, from Fig. 12, the displacements in the out-of-plane direction (i.e. along the y direction) are about 60% larger (corresponding to a ratio of 2.8/1.8 = 1.6 based on the peak values from Fig. 12) in the N-E (i.e. near EP8, refer to Fig. 4) corner than that in the S-E corner (i.e. near EP5, refer to Fig. 4) of the East wall. This observation together with a larger number of out-of-plane deformation cycles and larger residual deformation somewhat explain the reason why the damage was observed in EP8 but not in EP5.

a) Proximity of the investigated building to a ground motion recording station

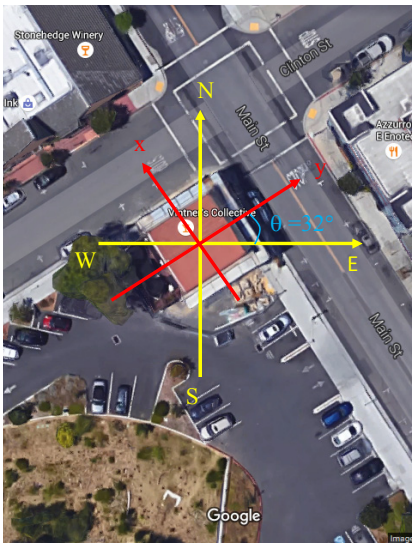

$A_y=A_{NS}\sin\theta+A_{EW}\cos\theta$

$A_x=A_{NS}\cos\theta-A_{EW}\sin\theta$

b) Transformation of the recorded ground motion to the building orthogonal axes

Fig. 5 – Station N016 from the USGS-NCSN strong motion network used in determining the ground motion for the NTHA of the analyzed building

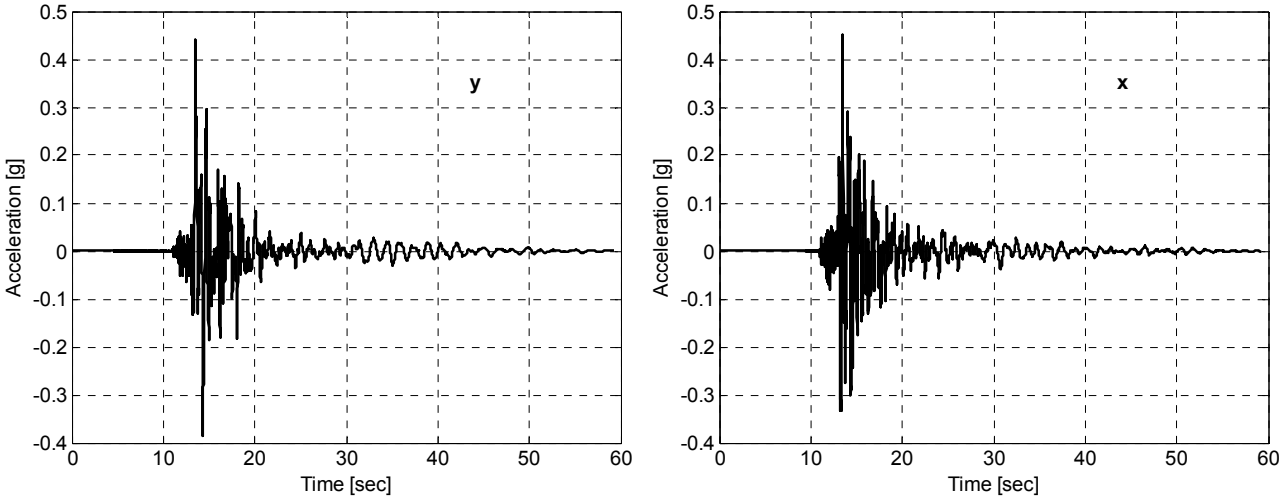

Fig. 6 – Ground accelerations along the two orthogonal directions of the investigated building

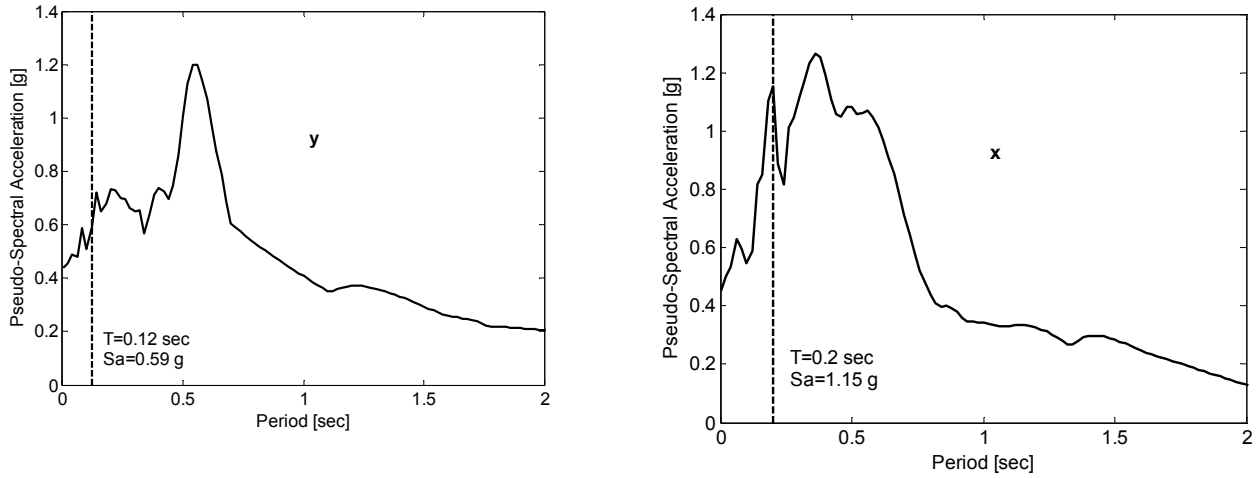

Fig. 7 – Response spectra of ground accelerations along the two orthogonal directions of the investigated building

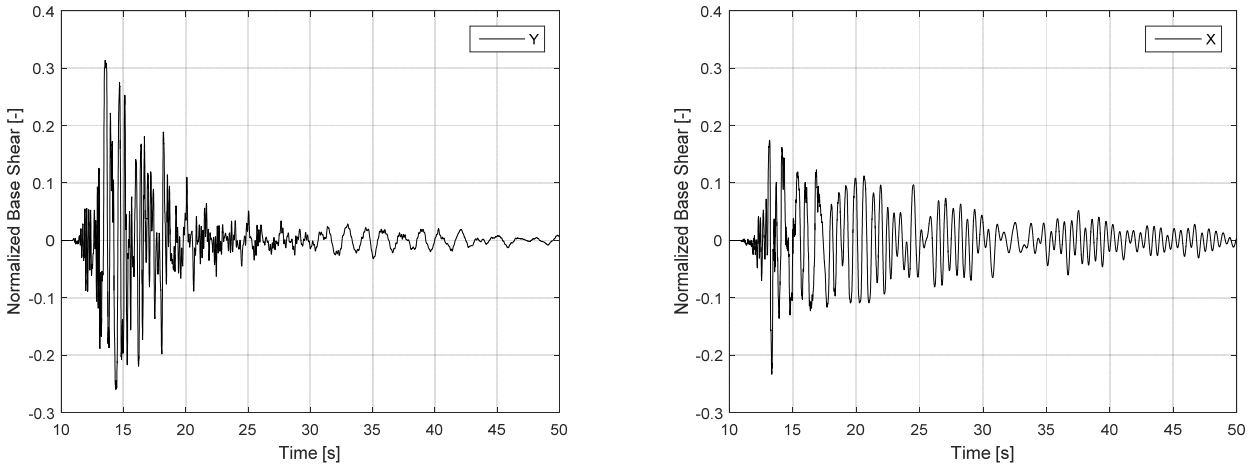

Fig. 8 – Time history of normalized base shear force in the two orthogonal directions of the building

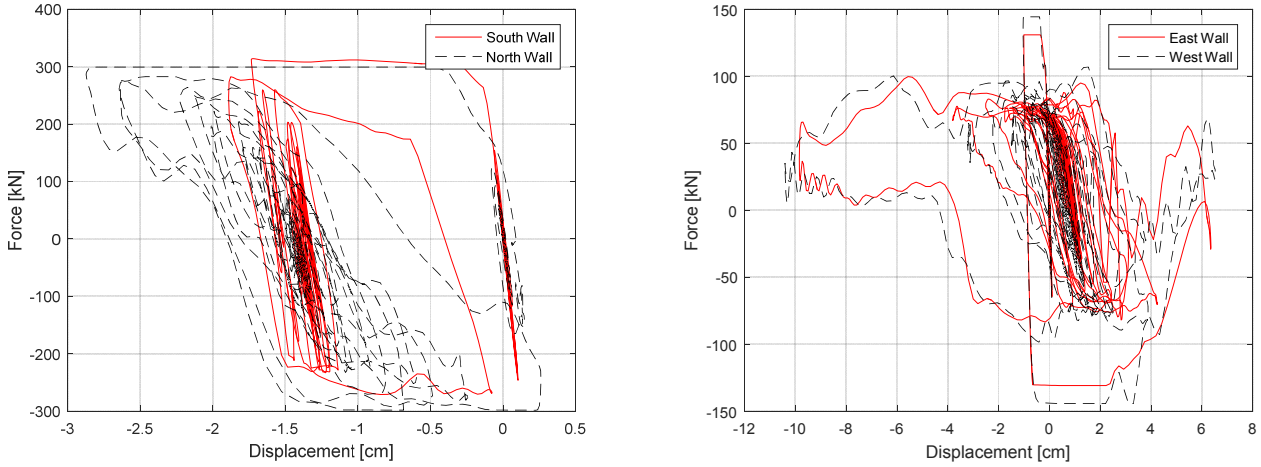

a) y direction b) x direction

Fig. 9 – Time history of normalized base shear force in the two orthogonal directions of the building

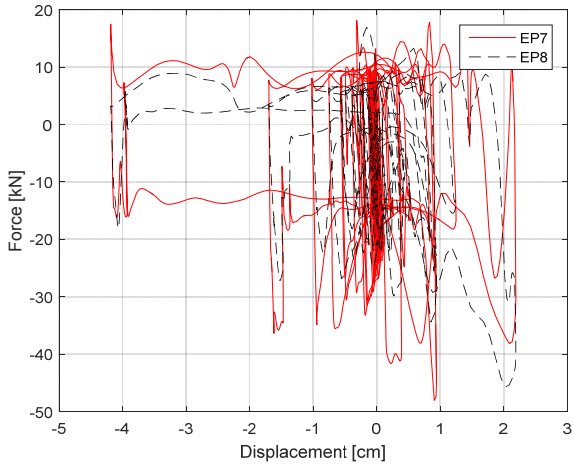

Fig. 10 – Force-displacement relationships of EP7 and EP8

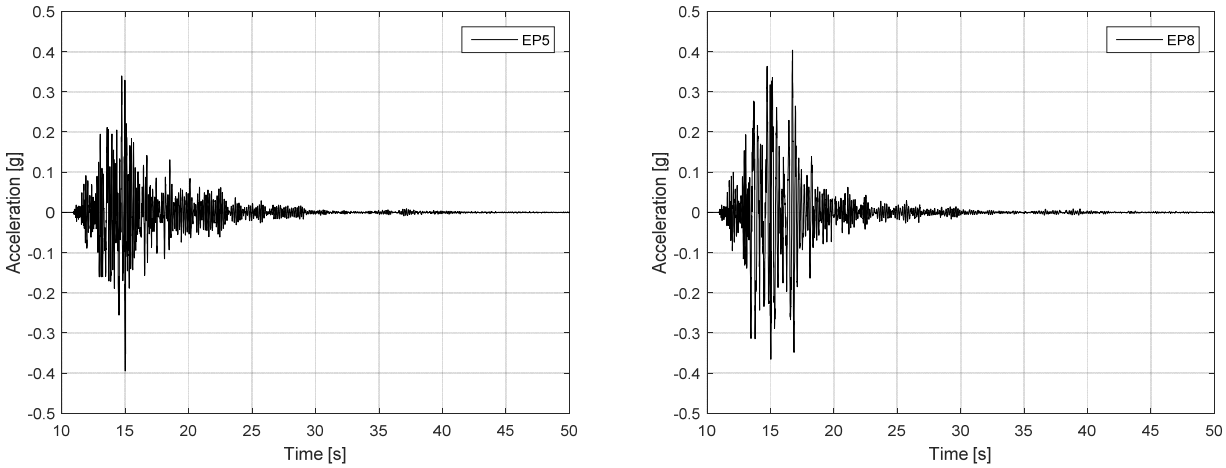

Fig. 11 – Out-of-plane (y direction) accelerations experienced by EP5 and EP8

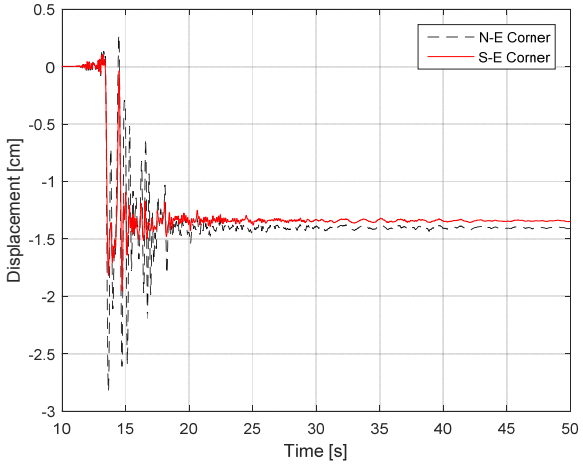

Fig. 12 – Out-of-plane (y direction) displacement of N-E (failed) and S-E (intact) corners of the East Wall

One other clear damage pattern that can be observed from the photographs of Figs. 3 and 4 is the shear cracks in the north wall piers NP1, NP2, and NP3. The in-plane force-displacement relationships of these piers are plotted in Fig. 13, where it is observed that all of the piers have reached their shear strength, explaining the observed shear cracks. The force-displacement relationship of pier SP2 is also plotted in Fig. 13, which shows that pier SP2 also reaches its capacity. However, the post-elastic displacements are smaller for SP2 than those of NP1, NP2, and NP3, which is a reasonable explanation why the shear cracks of the north piers are visible, while those of the south are not detected in the photographs of Fig. 3.

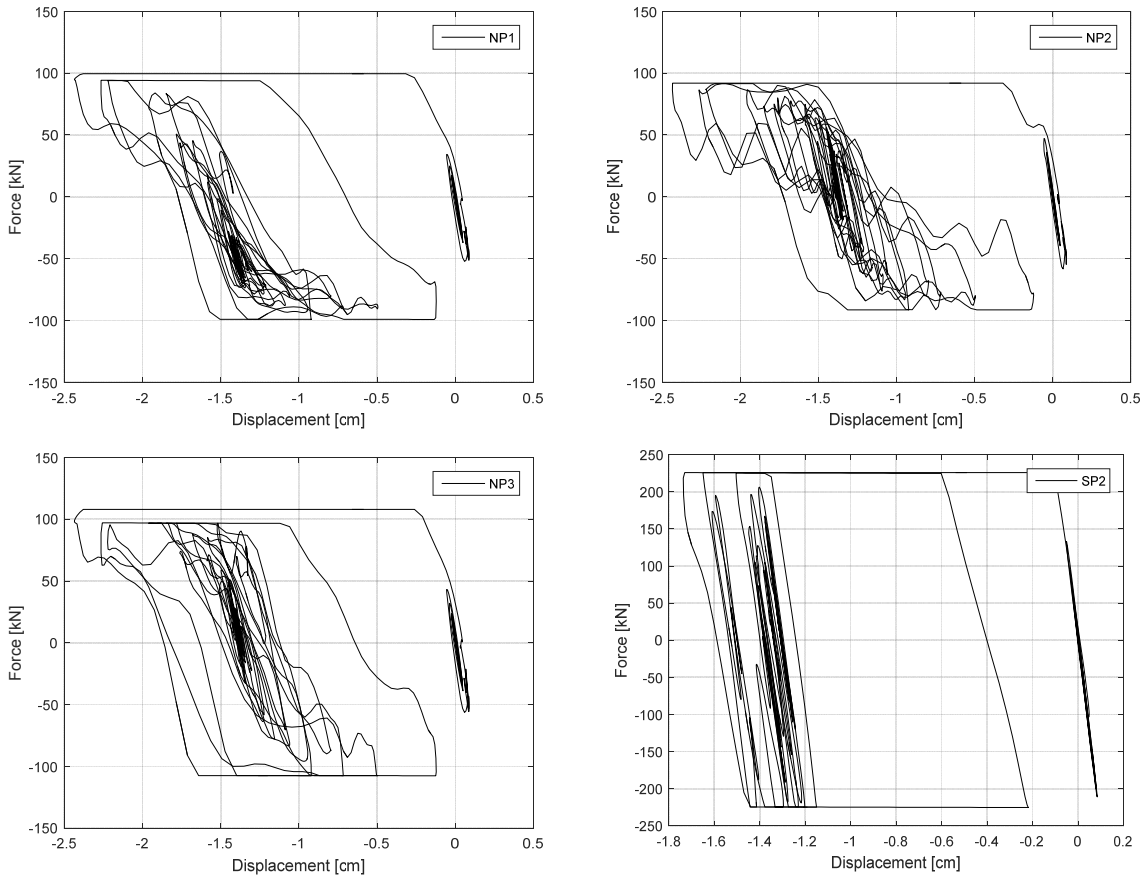

Fig. 13 – In-plane force-displacement relationships of the piers in the south and north walls

Finally, the acceleration time histories on the first floor along the four walls are plotted in Fig. 14, where differences between the accelerations on the north and south sides and between those on the east and west sides indicate the presence of torsion. These accelerations are large enough to lead to nonstructural content damage, such as falling of wine bottles or other sales items in the store, which would have not only led to economic losses but also injuries, had the earthquake occurred during day time.

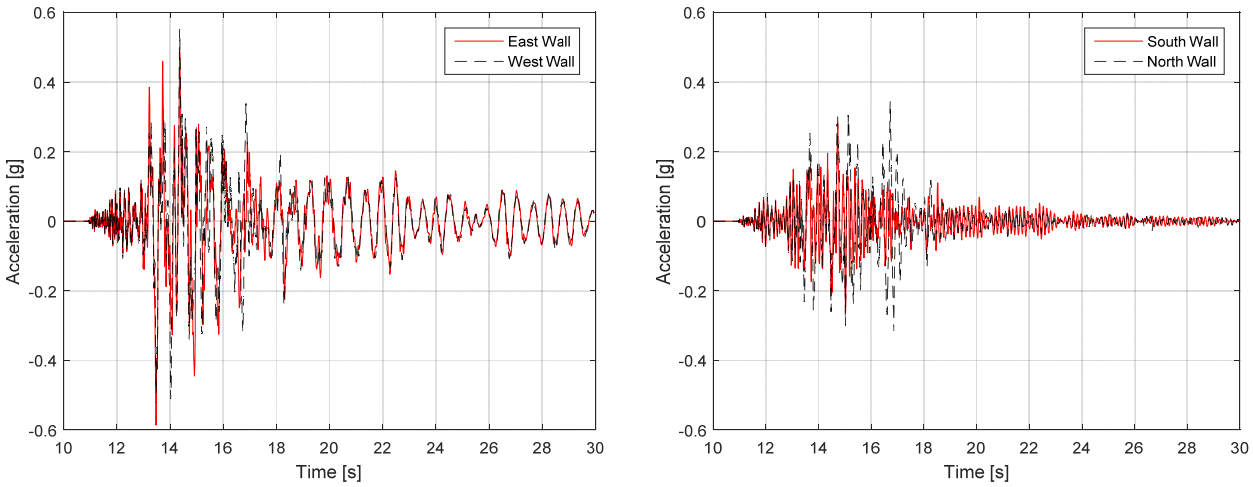

Fig. 14 – Time histories of first floor accelerations

6. Summary and Conclusions

The seismic response of an unreinforced masonry historical building damaged during the 2014 South Napa earthquake was discussed and reproduced in this paper. Starting from the geometrical observations collected via a laser scanner, a 3D finite element model was developed in the OpenSees framework. The equivalent frame method was adopted for the discretization of the masonry continuum, allowing to perform nonlinear time history analyses with a reasonable computational cost. Nonlinear displacement-based beam-column elements, with fiber discretization over the cross section, were adopted to represent the piers and spandrels of the masonry walls. The results of the analyses showed a complex dynamic response of the structure, characterized by highly nonlinear deformations and progressive reduction of the strengths. In-plane force-displacement relationships in North-South (x) direction were defined by a degrading behavior. On the other hand, the response in East-West (y) direction was governed by bed joint sliding that overcame the defined shear capacity. Both of these results are in agreement with the partial failure in the east wall and with the cracks of the piers of the north and south walls. Torsional effects, due to stiffness difference between the north and south walls, were also captured by the computational model. The resulting larger demand of displacement in y direction (out-of-plane) at the N-E corner of east wall is a possible reason for the higher level of damage in comparison to S-E corner. Finally, the increased floor accelerations due to torsion indicate damage risk for contents, in terms of non-structural components and sales items.

7. Acknowledgements

The laser scans were collected during the operations of NEES facilities at the University of California, Berkeley, which was supported by the National Science Foundation (NSF).

8. References

[1] National Park Service (2013): http://focus.nps.gov/AssetDetail/NRIS/74000540.

[2] Leica Geosystems, AG. (2015): Cyclone Version 9.1.

[3] MathWorks, Inc. (2015): Matlab Version 15b.

[4] Roca P, Molins C, Mari AR (2005): Strength capacity of masonry wall structures by the equivalent frame method. *Journal of Structural Engineering ASCE*, **131**(10), 1601-1610.

[5] Tomazevic (1987): Dynamic modelling of masonry buildings: Storey mechanism model as a simple alternative. *Earthquake Engineering & Structural Dynamics,* **15**(6), 731-749.

[6] Magenes G, Della Fontana A (1998): Simplified non-linear seismic analysis of masonry buildings. *Proceedings of the British Masonry Society,* **8**, 190-195.

[7] Lagomarsino S, Penna A, Galasco A, Cattari S (2013): TREMURI program: An equivalent frame model for the nonlinear seismic analysis of masonry buildings. *Engineering Structures,* **56**, 1787-1799.

[8] Belmouden Y, Lestuzzi P (2009): An equivalent frame model for seismic analysis of masonry and reinforced concrete buildings. *Construction and Building Materials,* **23**(1), 40-53.

[9] Marques R, Lourenco PB (2011): Possibilities and comparison of structural component models for the seismic assessment of modern unreinforced masonry buildings. *Computers and Structures,* **89**, 2079-2091.

[10] FEMA 306 (1998): Evaluation of earthquake damaged concrete and masonry wall buildings. *Federal Emergency Management Agency*, Washington, DC, USA.

[11] CNR-DT 212/2013 (2014): Reliability assessment for the seismic safety of existing buildings. *National Research Council* (*CNR*), Rome, Italy (in Italian).

[12] OpenSees (2000): Open system for earthquake engineering simulation. *Pacific Earthquake Engineering Research Center* (*PEER*)*,* University of California Berkeley, CA, USA.

[13] Mander JB, Priestley MJN, Park R (1988): Theoretical stress-strain model for confined concrete. *Journal of Structural Engineering ASCE,* **114**(8), 1804-1825.

[14] Augenti N, Parisi F (2010): Constitutive models for tuff masonry under uniaxial compression. *Journal of Materials in Civil Engineering ASCE,* **22**(11), 1102-1111.

[15] Liang X, Mosalam KM, Günay, S. (2016): Direct Integration Algorithms for Efficient Nonlinear Seismic Response of Reinforced Concrete Highway Bridges. *Journal of Bridge Engineering*, 04016041

[16] Mosalam KM, Liang X, Günay S, Schellenberg, A. (2013): Alternative Integrators and Parallel Computing for Efficient Nonlinear Response History Analyses. *COMPDYN 2013, 4th ECCOMAS Thematic Conference on Computational Methods in Structural Dynamics and Earthquake Engineering*, M. Papadrakakis, V. Papadopoulos, V. Plevris (eds.), June 12-14, 2013, Kos Island, Greece.